# Growth of boundary-layer streaks due to free-stream turbulence

Pierre Ricco [a,*], Edmond J. Walsh [b], Flavio Brighenti [c], Donald M. McEligot [d,e]

[a] *Department of Mechanical Engineering, University of Sheffield, Sheffield, S1 3JD, UK*

[b] *Department of Engineering Science, University of Oxford, Oxford, OX2 0ES, UK*

[c] *Karlsruhe Institute of Technology, Institute for Technical Physics, Campus North, Karlsruhe 76344, Germany*

[d] *Mechanical Engineering Department, University of Idaho, Idaho Falls, Idaho, 83401, USA*

[e] *Aerospace and Mechanical Engineering Department, University of Arizona, Tucson, Arizona, 85721, USA*

**Abstract**

**Accepted for publication in Int. J. Heat Fluid Flow.**

The growth of laminar boundary-layer streaks caused by free-stream turbulence encountering a flat plate in zero-pressure-gradient conditions is investigated experimentally in a wind tunnel and numerically by solving the unsteady boundary-region equations. A comparative discussion amongst the most relevant theoretical frameworks, such as the Goldstein theory, the Taylor-Stewartson theory, the optimal-growth theory and the Orr-Sommerfeld theory, is first presented and parallels and complimentary aspects of the theories are pointed out to justify the use of the Goldstein theory in our study. The statistical properties of the positive and negative fluctuations of the laminar streaks are discussed, showing how the total time average of the boundary-layer fluctuations masks the true character of the disturbance flow and revealing that the maximum values and the root-mean-square of positive and negative fluctuations grow downstream at the same rate. The downstream growth rate of the low-frequency disturbances and the decay rate of the high-frequency disturbances are also computed for the first time. The numerical solutions of the unsteady boundary-region equations are compared successfully with the streak profiles

* Corresponding author

measured in the wind tunnel and with direct numerical simulation results available in the literature.

*Key words:* Boundary layers, transition to turbulence

## 1 Introduction

The topic of boundary-layer transition to turbulence is of extreme importance in the aeronautical, turbomachinery, and maritime industries because of the much higher wall friction drag exerted by the flow in the turbulent regime than in the laminar regime. It is therefore paramount for scientists and engineers to understand the physical causes of such a process, to predict its occurrence, and to control it to delay the breakdown of the flow to turbulence.

### *1.1 The laminar streaks and bypass transition*

Boundary-layer transition in the presence of a low level of free-stream turbulence is widely acknowledged to be initiated by exponentially growing Tollmien-Schlichting (TS) waves [49], but for free-stream turbulence levels which are comparable to and larger than about 1%, the laminar-flow breakdown appears to be linked to streamwise-elongated regions of high and low streamwise velocity which dominate the boundary-layer core. These structures have been termed laminar streaks, breathing modes, or Klebanoff modes [22, 21]. The streaks are believed to be responsible for bypass transition in which the role of unstable TS waves, as predicted by the linear stability theory, is likely to be marginal or even irrelevant [33]. The breakdown of the Klebanoff modes is caused by secondary instability and occurs abruptly along the flat plate. In most industrial flow scenarios, free-stream flows impinging on rigid surfaces are common and bypass transition is the norm. This has spurred a growing interest in the Klebanoff modes over the last twenty years.

A complete understanding of the bypass transition has not been attained, despite research efforts based on experiments [33, 11, 16, 17, 37, 39], numerical simulations [20, 24, 38], and theoretical analysis [26] (hereafter referred to LWG99) [28, 60, 44, 13]. The boundary layer has been revealed to act as a filter for the full-spectrum free-stream vortical disturbances, thereby allowing low frequency disturbances to penetrate into the boundary-layer core and to amplify significantly, whilst preventing high-frequency fluctuations from growing downstream. The high-frequency disturbances therefore remain confined in the outer portion of the shear layer. As the breakdown mechanism is still unclear, prediction of transition subjected to free-stream turbulence for aeronautical and turbomachinery applications relies heavily on empirical models based mainly on experimental data [35, 34, 1].

### *1.2 Theoretical frameworks for the laminar streaks*

A mathematical description of the Klebanoff modes has been developed by Goldstein and co-workers (LWG99), [60, 58, 57, 13]. The Goldstein theory accounts for the presence of free-stream disturbances that are responsible for the generation and downstream development of the streaks. It is remarked that the correct description of the free-stream vortical disturbances is essential for capturing the streak dynamics. The key physical mechanism for the formation of the Klebanoff modes is revealed: there is an interaction between the boundary-layer disturbances and the free-stream fluctuations and the free-stream flow is continuously affected by the downstream growth of the boundary layer. Only the wall-normal and spanwise velocity components of the free-stream disturbances are relevant for the formation and growth of large streamwise-velocity streaks in the boundary-layer core, while the free-stream streamwise velocity component plays a secondary role. Ricco [42] (hereafter referred to as R9), by adopting LWG99's asymptotic approach, showed that a balance between the free-stream pressure fluctuations and the streamwise velocity fluctuations is relevant for the formation of the streak fluctuations in the outer part of the boundary layer. A realistic streak profile along the whole wall-normal extent of the boundary layer was obtained by R9 and good agreement with the experimental data by Westin *et al.* [56] was shown. Ricco & Dilib [43] employed R9's approach to show that the peak of the streak amplitude in the boundary-layer core may be completely suppressed if intense wall transpiration is applied and Ricco and co-authors [47, 46, 45] have studied the Klebanoff modes in compressible boundary layers.

Other theories have been put forward to describe the laminar streaks. The three most relevant ones are discussed below.

– *The Taylor-Stewartson theory*
  The first attempt to model the wall-normal profile of the streaks is due to Taylor [52]. He recognized that the streak profile can be described in terms of a small spanwise modulation of the boundary layer thickness. Stewartson [50] translated Taylor's original idea in mathematical form by a simple perturbation of the boundary-layer thickness and showed that the root-mean-square (rms) profile of the streamwise velocity fluctuations agrees well with $u = \eta F''$ (where $F(\eta) = \psi/\sqrt{2\nu U_\infty x}$ is the Blasius function [5], $\psi$ is the boundary-layer streamfunction, $\nu$ is the kinematic viscosity, $U_\infty$ is the free-stream velocity, $x$ is the streamwise coordinate, $\eta = y/\delta$ is the scaled wall-normal coordinate and $\delta$ is the laminar boundary-layer thickness).
– *The optimal-growth theory*
  This approach was first developed by Luchini [28] and Andersson *et al.* [2]. The objective of the analysis is to find the initial velocity profile near the leading edge that maximizes a specified cost function, which may represent the energy of the perturbation within the entire viscous layer or at a specified downstream distance. When the peak disturbance is normalized, the wall-normal profile agrees well with the Taylor-Stewartson mode and with the

experimental rms profiles of the streamwise velocity in the boundary-layer core [56, 33], although no comparison on the downstream evolution has been carried out.

The three-dimensional boundary-layer equations (which coincide with LWG99's boundary-region equations) describe the flow. The crucial difference with the Goldstein theory is the specification of the *initial* and *free-stream boundary* conditions. In the optimal-growth theory, the free-stream disturbances, which cause the formation and downstream growth of the streaks, are not included in the formulation. Homogeneous outer boundary conditions are imposed on the streamwise and spanwise velocity components, i.e., the boundary-layer disturbances vanish as the boundary-layer wall-normal coordinate approaches the free stream. As a consequence, the initial conditions in the general three-dimensional case cannot be found before starting the numerical integration. A special case is represented by disturbances with spanwise wavelengths which are much larger than the boundary-layer thickness. For this case the downstream growth rate is $x^{0.213}$ [27].

Goldstein's asymptotic analysis instead allows the mathematically precise and unambiguous specification of both the *initial* conditions, which describe the flow in the proximity of the leading edge of the plate from which the downstream evolution of the streaks commences, and the *outer (free-stream)* boundary conditions, which characterize the flow in the outer portion of the boundary layer and its interplay with the free-stream disturbance flow. The correct mathematical representation of both conditions is crucial because they uniquely determine the streak dynamics. The initial conditions are unequivocally linked with the outer flow through the matched asymptotic expansion approach. The key point here is that their mathematical relation synthesizes the physical interaction between the oncoming free-stream disturbance flow and the boundary layer near the leading edge. The initial and outer flow are therefore fully consistent and their mathematical relationship is found by expanding the solution of the outer flow through a series (LWG99). This series in turn leads to a regular power-series expansion of the initial flow near the leading edge. An asymptotic composite solution for the wall-normal streak profile at small downstream distances is then obtained. This profile is used to initiate the downstream computation of the parabolic boundary-region equations.

In the optimal-growth theory, the mathematical relationship between the boundary-layer perturbation flow and the free-stream flow is not established. The initial conditions *are therefore unknown a priori* and thus cannot be specified as an *input* to the calculations. The initial condition is computed as an *output* through the optimization procedure, together with the streak flow field downstream. As elucidated by Wundrow & Goldstein [60], the effectiveness of the optimal growth theory to model the early stage of bypass transition is thus questioned.

As the oncoming free-stream perturbation flow is neglected in the frame-

work, the "optimal" flow is obviously not dependent on the free-stream flow characteristics (such as wavelength, frequency, energy spectrum) as it is in experiments and in the Goldstein theory. Instead, the final solution (initial and downstream flows) depends on the arbitrary choices of the cost function to be maximized (velocity components to be included, kernel), on the initial location, and on the final location of the domain inside which the cost function is maximized. Through the optimal-growth theory, the characteristics of the free-stream flow, such as its wavelength, frequency, intensity, and spectrum, cannot be linked with the downstream growth of the streaks, with the location of their secondary instability and with the dynamics of bypass transition.

Furthermore, the optimal-growth theory predicts the streaks to be steady, while experimental studies have shown that the Klebanoff modes are unsteady and their breakdown occurs intermittently in time. LWG99's initial condition analysis shows that the unsteadiness can be neglected only in the very proximity of the leading edge. The importance of the unsteadiness has been confirmed by Wu & Choudhari [57].

The theoretical and numerical work by Higuera & Vega [18] showed that the spanwise wavenumber can be eliminated from Luchini [28]'s and Andersson *et al.* [2]'s equations, thereby proving that the optimization technique employed to search for the optimal mode is not necessary. As Higuera & Vega considered the steady problem only and did not take into account the distributed free-stream forcing, their scaled solution is the analogue of the asymptotic quasi-steady solution found by LWG99 (bottom of page 183 in LWG99) for the case of vanishing free-stream fluctuations. Further investigations of the steady boundary-layer streaks without free-stream perturbations have been carried by Martin & Martel [31, 32].

– *The Orr-Sommerfeld theory*

The continuous spectra of the Orr-Sommerfeld and Squire equations has been used extensively to describe the small-amplitude streaks generated by free-stream turbulence. Differently from the Goldstein theory and the optimal-growth theory (for which the equations of motions are parabolic and account for the downstream flow evolution), the Orr-Sommerfeld theory is *local* because the disturbance flow only depends on the mean boundary-layer flow at the specified downstream location and not on the evolution of the flow from the proximity of the leading edge. This model has also been employed widely to synthesize the inflow in DNS of bypass transition [20, 6].

The use of the Orr-Sommerfeld theory to generate the inflow condition for DNS simulations has recently been proved to be invalid by Dong & Wu [10]. Non-parallel terms are not retained in the formulation as the flow is assumed to be parallel. Dong and Wu showed, amongst other things, that neglecting non-parallel terms causes:

*i*) a spurious "Fourier-modes entanglement", that is, a physically unrealistic interaction between free-stream modes which prevents the specification of all possible free-stream disturbances.

*ii*) a free-stream flow which is a result of the boundary-layer computation and is not imposed *a priori* as the oncoming free-stream flow, for example as it happens in a wind tunnel where the free-stream flow is produced by an upstream turbulence-generating grid. The crucial point here is that, in a laboratory, the oncoming free-stream disturbance flow may obviously exist even if the flat plate does not, while the Orr-Sommerfeld theory leads to the absurd result that the free-stream flow is present only if the boundary-layer flow is modelled.

*iii*) unrealistic high magnitudes of the free-stream perturbation velocity, which have been arbitrarily "smoothed" by an artificial function to lower values when the Orr-Sommerfeld and Squire modes have been used as inflow for DNS (refer to page 174 of Brandt *et al.* [6]).

The mathematical representation of the free-stream disturbance flow through the Orr-Sommerfeld and Squire spectra is therefore called into question by Dong & Wu [10] as this spectrum is a by-product of the linear operator and has no physical meaning.

It is curious to note that the Orr-Sommerfeld theory and the optimal-growth theory are somewhat complimentary as the most distinguished features of one theory are absent in the other theory. The optimal-growth theory accounts for the initial conditions, nonlocality, nonparallel effects of the streaks, but does not model free-stream vortical disturbances and unsteadiness. Reversely, the Orr-Sommerfeld theory does model the effect of free-stream turbulence and unsteadiness, but neglects nonparallel and nonlocal effects, and thus the downstream evolution of the perturbation and the influence of the flow near the leading edge. The Goldstein theory instead includes all these features, which are all essential to characterize the streak dynamics.

There is a further parallel between the optimal-growth theory and the Orr-Sommerfeld theory. Neither the initial conditions in the optimal-growth theory nor the free-stream flow in the Orr-Sommerfeld theory are inputs to the computation: they are results in both theories. On the contrary, the initial and free-stream conditions are inputs in the Goldstein theory. Table 1 schematically summarizes the main features of the four theories discussed.

### *1.3 Objectives and structure of the paper*

The objectives of the present study are discussed as follows.

- *Evolution of positive and negative fluctuations*
  A statistical characterization of the positive and negative (with respect to the mean) fluctuations of the laminar streaks is still lacking. To address this point, accurate wind-tunnel measurements have been performed in a flat-plate laminar boundary layer in the presence of a medium level of free-stream turbulence. Another objective is to study how the most energetic instantaneous motions evolve downstream and how their characteristics relate to time-averaged statistics.

Table 1
Schematic description of main features of theoretical frameworks. Terms in italics denote the differences from Goldstein theory (refer to discussion in §1.2).

| **Theory** | **Locality** | **Initial conditions** | **Free-stream conditions** | **Unsteadiness** | **Nonparallel** |
|---|---|---|---|---|---|
| **Goldstein theory** (LWG99,[57],R9) | Non-local | Matched asymp. expan. | Matched asymp. expan. | Yes | Yes |
| **Taylor-Stewartson theory** [52, 50] | *Local* | *Absent* | *Absent* | *No* | *Yes* |
| **Optimal-growth theory** [28, 2] | Non-local | *Optimal initial* | *Absent* | *No* | Yes |
| **Orr-Sommerfeld theory** [20, 6] | *Local* | *Absent* | *Fourier-modes entangl.* | Yes | *No* |

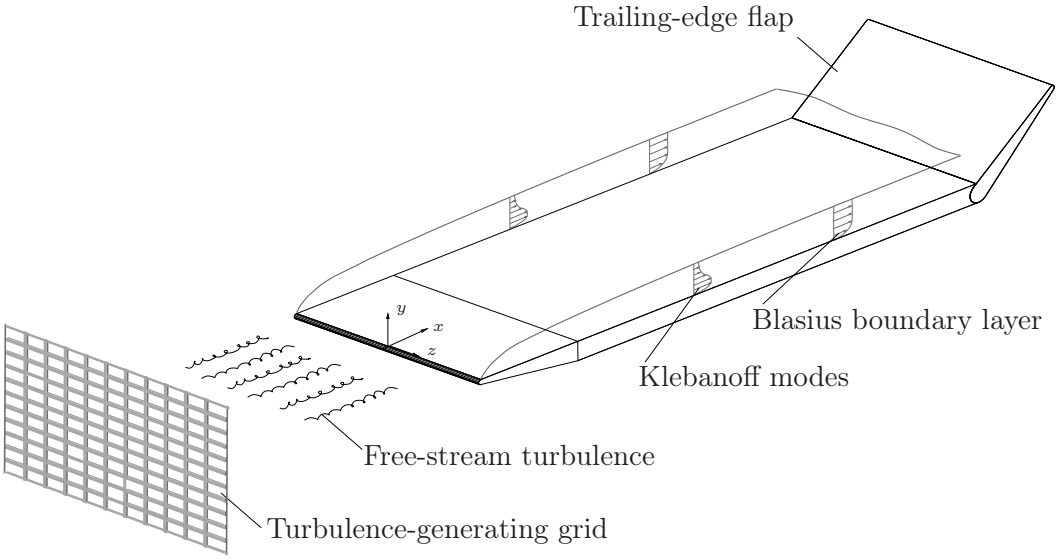


Figure 1. Wind-tunnel test section.

- *Downstream growth of streaks at different frequencies*
  The second objective is to investigate how streaky structures corresponding to different frequencies grow or decay downstream.
- *Assessment of the theory*
  Our wind-tunnel data and the DNS results by Wu & Moin [59] are used to assess the theoretical frameworks by LWG99 and R9. The objective is to compare the profiles obtained through our boundary-region solutions with the measured wall-normal profiles of the streamwise velocity at a specified frequency and with the DNS profiles. R9 compared his numerical results with the data by Westin *et al.* [56], but further comparison is needed to confirm the validity of the theoretical approach.

Section §2 describes the wind-tunnel facility and the experimental procedures, while the mathematical formulation is presented in §3. The experimental results are discussed in §4. Section §5 contains the comparisons between our boundary-region results and our experimental data and the DNS data by Wu & Moin [59]. Section §6 summarizes the results.

## 2 Experimental procedures

In this section, the wind tunnel apparatus, the experimental procedures, and the characteristics of the free-stream flow are presented. More details of the experimental procedures can be found in the thesis by Brighenti [7].

### *2.1 Wind-tunnel apparatus and hot-wire anemometry measurements*

A zero-pressure-gradient laminar boundary layer flow with a mean free-stream velocity $U^*_\infty = 3.1 \pm 0.03$ m/s has been investigated experimentally by a single hot-wire anemometer in a non-return wind tunnel at the Stokes Research Institute at the University of Limerick. The superscript $*$ hereinafter indicates dimensional quantities. The experiments have been conducted at a pressure of

99430 Pa and at a temperature of 21.2°C, maintained constant to within 0.3°C. The kinematic viscosity of air at these conditions was $\nu^*$=1.5·10$^{-5}$ m$^2$/s.

Figure 1 shows a schematic diagram of the experimental apparatus. The free-stream flow was induced by a 70kW motor-driven centrifugal fan at the inlet of the wind tunnel. The test surface was a flat 10-mm-thick aluminium plate and the test section measured 1 m in length and 0.3 m in width and height. The leading edge was semi-cylindrical with a radius of about 1 mm. As shown in figure 1, the top surface of the plate was parallel to the mean-flow direction and its thickness increased linearly from 2 mm at the leading edge to 10 mm at a downstream location of 100 mm. The thickness remained constant downstream of this location. References [55] and [7] give further details on the apparatus and the measurements along planes at different spanwise locations, which show that the mean flow can be considered two-dimensional. The downstream part of the plate was a trailing-edge flap, which allowed positioning the stagnation line at the leading edge and avoiding separation. Walsh *et al.* [55] carried out liquid-crystal shear-stress measurements and china clay visualization to demonstrate that a 45° flap angle helped guarantee the attached flow in the proximity of the leading edge. As also demonstrated by Brighenti [7] on his pages 35-36, the choice of this angle also ensured that zero-pressure-gradient conditions were achieved in the measurement region and that the laminar boundary layer showed excellent agreement with the Blasius laminar solution.

The streamwise mean and fluctuating velocities were measured using an A.A. Lab Systems AN-1005 constant temperature hot-wire anemometer operated at an overheat temperature of 250°C. A Dantec 55P14 single right-angle probe, connected to a Digiplan Pk 3 stepper motor drive, was used. A traversing system which allowed increments of 10 µm was employed for measurements along the test section and normal to the plate. The hot-wire calibration was carried out in the range 0-20 m/s by fitting the data using King's law. This range exceeds the one of the measurements presented herein because the latter are part of a broader study on boundary-layer transition, documented in the thesis by Brighenti [7]. The distance between the surface and the first wall-normal position $y$ was estimated by extrapolation of the Blasius solution profile, after discarding points strongly affected by heat conduction through the wall. Hot-wire measurements were taken for a number of streamwise positions with sampling periods of 20 s. This duration corresponded to a minimum of about 10 independent realizations, estimated through the representative lowest frequency measured, i.e., about 0.5 Hz. The sample frequency was 10 kHz, low-pass filtered at 3.8 kHz.

The data presented are for Reynolds numbers up to $Re_\theta = U^*_\infty \theta^*/\nu^* = 161$, where $\theta^*$ is the momentum thickness. Although we have not conducted measurements in the transition region and therefore we have not computed the exact location of the beginning of the transition process, our last measurement

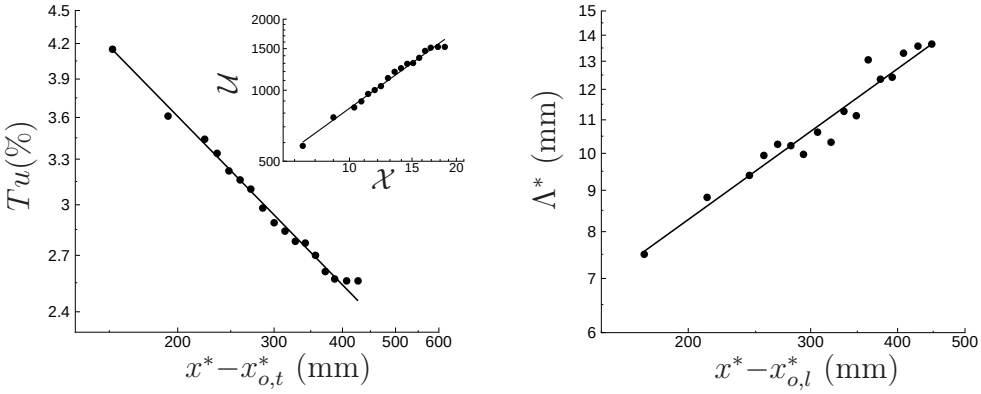


Figure 2. Decay of free-stream turbulence intensity $Tu(\%)$ (left) and growth of integral length scale $\Lambda^*$ (right) for grid generated turbulence in log-log scale. The straight lines are the algebraic expressions (1) and (3) for $Tu(\%)$ and $\Lambda^*$, respectively. The grid is 280 mm upstream of the leading edge of the plate and the first data point is at the leading edge. Inset in left graph: $u^*_{rms}$ scaled as in equation (2), i.e., $\mathcal{U}$ and $\mathcal{X}$ are the left- and the right-hand-side in (2), respectively.

location was upstream of predicted transition locations, i.e., $Re_{\theta,tr}$ =169.5, obtained through the widely used correlation formula $Re_{\theta,tr} = 400Tu(\%)^{-5/8}$ [34] and $Re_{\theta,tr}$ =188.5, found by use of $Re_{\theta,tr} = 460Tu(\%)^{-0.65}$ [19].

### *2.2 Free-stream turbulence*

The free-stream turbulence was generated by the uniform flow passing through a perforated plate with square openings and positioned perpendicularly to the oncoming flow between the inlet contraction and the test section. The bar thickness was $t^*_b$=2.6 mm and the distance between adjacent openings was also 2.6 mm along both the wall-normal and the spanwise directions. The mesh width $M^*$, i.e., the length of each side of the square opening, was 22 mm. The grid solidity, measured as the percentage of solid area with respect to the total grid area, was 23%, i.e., below 50% in order to avoid flow instabilities due to jet coalescence [14, 48]. The leading edge of the plate was located at 280 mm, i.e., at about $13M^*$ downstream of the grid, a sufficient distance to avoid the intense anisotropic character of the turbulence in the proximity of the grid [48].

The free-stream turbulence intensity was $Tu(\%) = 100u^*_{rms}/U^*_\infty$=3.95% at the leading edge, where $u^*_{rms}$ indicates the rms of the streamwise velocity fluctuations,

$$u^*_{rms} = \sqrt{\overline{[u'^*(t^*)]^2}},$$

where $u'^*(t^*) = u^*(t^*) - \overline{u^*(t^*)}$, $u^*(t^*)$ indicates the instantaneous streamwise velocity, and the symbol $\bar{\cdot}$ denotes the time average. The turbulence decay can be represented through the following algebraic expression,

$$Tu(\%) = \mathcal{C}_t(x^* - x^*_{o,t})^{-n}, \tag{1}$$

where $x^*$ is the streamwise distance from the leading edge and $x^*_{o,t}$ is the virtual streamwise position of the grid for the turbulence intensity, which accounts for the fact that the origin of the decaying turbulence may not agree with the actual location of the grid. Figure 2 (left) shows the turbulence intensity data. The method of least squares gives $\mathcal{C}_t = 53$, $n = 0.51$ and $x^*_{o,t} = -152$ mm, i.e., $x^*_{o,t}/M^* = -6.9$. The value of the virtual origin was found to be smaller than the actual origin also by Fransson *et al.* [11] and is typically in the range of $0-20x^*_{o,t}/M^*$ upstream of the leading edge [36]. The value for $n$ matches well $n = 0.5$ for isotropic turbulence, found by Tennekes & Lumley [53]. Data for $n$ reported in the literature are in the range $0.5 - 0.665$ [9, 36, 61, 54]. The accurate data measured by Fransson *et al.* [11] showed very good agreement with the analytical curve when $n = 0.6$ was used. The scatter in the values for $n$ has generally been attributed to the dependence of grid turbulence on the initial conditions [12, 23].

The inset of figure 2 (left) shows the same $u^*_{rms}$ data scaled as in the seminal paper by Comte-Bellot & Corrsin [9], i.e.,

$$\left(\frac{U^*_\infty}{u^*_{rms}}\right)^2 = \mathcal{A}\left(\frac{x^*}{M^* + t^*_b} - \frac{x^*_1}{M^* + t^*_b}\right)^{n_c}, \tag{2}$$

where $\mathcal{A} = 68$, $x^*_1/(M^* + t^*_b) = 4$, and $n_c = 1.1$ are found through the method of least squares. These values are within the ranges found in the literature, i.e., $\mathcal{A} = 13 - 71$, $x^*_1/(M^* + t^*_b) = 1 - 9$, $n_c = 1 - 1.39$ (refer to tables on page 666 in Comte-Bellot & Corrsin [9]).

The streamwise integral time scale of the free-stream turbulence was computed through the autocorrelation of the time signal $u^*(t^*)$ of the streamwise velocity fluctuations as follows

$$\Lambda^*_t = \int_0^\infty \frac{\overline{u'^*(t^*)u'^*(t^* + \tau^*)}}{u^{*2}_{rms}} \mathrm{d}\tau^*. \tag{3}$$

Taylor's hypothesis of frozen turbulence [51] was employed to obtain the integral length scale from the integral time scale as follows: $\Lambda^* = \Lambda^*_t U^*_\infty$ (refer to Pope [40] on page 224). Figure 2 (right) shows the integral length scale data. The integral scale was $\Lambda^* = 7.5$ mm at the leading edge of the plate and increased downstream as the turbulence decayed, as widely reported in the literature [11]. The following analytical expression may be employed

$$\Lambda^*(\mathrm{mm}) = \mathcal{C}_l(x^* - x^*_{o,l})^m.$$

The method of least squares gives $\mathcal{C}_l = 0.31$, $m = 0.62$ and $x^*_{o,l} = -173$ mm ($x^*_{o,l}/M^* = -7.9$) for the virtual streamwise position of the grid for the integral length scale, which is close to the value of the virtual origin for the turbulence

intensity. The value for $m$ is comparable with $m = 0.5$ proposed by Laws & Livesey [25].

## 3 Mathematical formulation

The mathematical framework by LWG99 and R9 is summarized in this section.

### *3.1 Free-stream flow and scaling*

As in the wind tunnel experiments, an incompressible flow of uniform velocity $U^*_\infty$ past a flat plate is considered. Superimposed on $U^*_\infty$ are statistically-stationary vortical fluctuations of the gust type, i.e., they are passively convected by the mean flow. The flow is described by Cartesian coordinates, i.e., by the vector $\mathbf{x} = x\hat{\mathbf{i}} + y\hat{\mathbf{j}} + z\hat{\mathbf{k}}$, where $x, y$ and $z$ define the streamwise, wall-normal, and spanwise directions, respectively. Lengths are scaled by $\lambda^*_z$, the characteristic spanwise wavelength of the gust, the velocities are scaled by $U^*_\infty$, the pressure by $\rho^* U^{*2}_\infty$, where $\rho^*$ is the density, and the time by $\lambda^*_z/U^*_\infty$.

The free-stream vorticity fluctuations are modelled as a superposition of sinusoidal disturbances:

$$\mathbf{u} - \hat{\mathbf{i}} = \epsilon \mathbf{u}_\infty(x - t, y, z) = \epsilon \hat{\mathbf{u}}^\infty \mathrm{e}^{i(\mathbf{k}\cdot\mathbf{x} - k_x t)} + c.c., \tag{4}$$

where $\hat{\mathbf{u}}^\infty = \{\hat{u}^\infty_x, \hat{u}^\infty_y, \hat{u}^\infty_z\}$, $\epsilon \ll 1$ indicates the gust magnitude, and *c.c.* denotes the complex conjugate. The problem is formulated for a single dominant Fourier component of the free-stream turbulence. Low-frequency (i.e., long-wavelength) disturbances with $k_x \ll 1$ are considered since these are the ones that can penetrate the most into the boundary layer. An asymptotically large Reynolds number $R_\lambda = U^*_\infty \lambda^*_z/\nu^* \gg 1$ is defined and the streamwise coordinate is scaled as $\overline{x} = k_x x = \mathcal{O}(1)$.

### *3.2 Mathematical description of the laminar streaks*

For the laminar boundary-layer flow over a flat plate, a similarity solution exists with the similarity variable defined as

$$\eta = y\sqrt{\frac{R_\lambda}{2x}} = y^*\sqrt{\frac{U^*_\infty}{2\nu^* x^*}}. \tag{5}$$

The mean flow solution is expressed as

$$U = F'(\eta), \quad V = (2xR_\lambda)^{-1/2}\left(\eta F' - F\right), \tag{6}$$

where the prime indicates differentiation with respect to $\eta$, and $U$ and $V$ represent the mean Blasius streamwise and wall-normal velocity components. It follows from the $x$-momentum equation that $F$ is governed by

$$F''' + FF'' = 0, \tag{7}$$

with boundary conditions $F(0) = F'(0) = 0$ and $F' \to 1$ as $\eta \to \infty$. The solution in the boundary layer is expressed as:

$$\{u, v, w, p\} = \{U, V, 0, -1/2\}$$

$$+\epsilon \left\{ \overline{u}_0(\overline{x}, \eta), \sqrt{\frac{2\overline{x}k_x}{R_\lambda}}\overline{v}_0(\overline{x}, \eta), \overline{w}_0(\overline{x}, \eta), \overline{p}_0(\overline{x}, \eta) \right\} \mathrm{e}^{i(k_z z - k_x t)} \; + \; c.c. + \ldots \quad (8)$$

The velocity and pressure disturbances are expressed as [15]

$$\left.\begin{aligned} \{\overline{u}_0, \overline{v}_0\} &= C^{(0)} \left\{\overline{u}^{(0)}, \overline{v}^{(0)}\right\} + (ik_z/k_x) C\{\overline{u}, \overline{v}\}, \\ \overline{w}_0 &= -(ik_x/k_z) C^{(0)} \overline{w}^{(0)} + C\overline{w}, \\ \overline{p}_0 &= (k_x/R_\lambda) C^{(0)} \overline{p}^{(0)} + i\kappa \left(k_x/R_\lambda\right)^{1/2} C\overline{p}, \end{aligned}\right\} \quad (9)$$

where

$$\kappa = \frac{k_z}{\sqrt{k_x R_\lambda}} = \frac{1}{\lambda_z^*}\sqrt{\frac{2\pi\nu^*\lambda_x^*}{U_\infty^*}} = \mathcal{O}(1), \quad (10)$$

$$C^{(0)} = \hat{u}_x^\infty + \frac{ik_x\hat{u}_y^\infty}{\sqrt{k_x^2 + k_z^2}} = \mathcal{O}(1), \quad C = \hat{u}_z^\infty + \frac{ik_z\hat{u}_y^\infty}{\sqrt{k_x^2 + k_z^2}} = \mathcal{O}(1). \quad (11)$$

The terms proportional to the components $\{\overline{u}, \overline{v}, \overline{w}, \overline{p}\}$ have been studied by LWG99 and represent the dominant part of the vorticity and pressure fluctuations in the core of the boundary layer. The terms proportional to the components $\{\overline{u}^{(0)}, \overline{v}^{(0)}, \overline{w}^{(0)}, \overline{p}^{(0)}\}$ indicate the second-order part in the boundary-layer core and the leading-order part of the Klebanoff modes at the outer edge of the boundary layer. They have been studied by R9. Both $\{\overline{u}^{(0)}, \overline{v}^{(0)}, \overline{w}^{(0)}, \overline{p}^{(0)}\}$ and $\{\overline{u}, \overline{v}, \overline{w}, \overline{p}\}$ satisfy the linearized unsteady boundary-region (LUBR) equations, which represent the asymptotic limit of the Navier-Stokes equations for disturbances with streamwise wavelength which is long compared with both the boundary-layer thickness and the spanwise wavelength. The condition for linearization is $\epsilon R_\lambda \ll 1$. The LUBR equations are given in LWG99 on page 180 and for brevity are not repeated here. The free-stream boundary conditions are given by expressions (5.28)-(5.31) on page 183 in LWG99 and by expressions (2.13) and (2.21)-(2.23) on pages 276 and 277 in R9. The initial conditions are given by expressions (5.24)-(5.27) on page 182 in LWG99 and by expressions (2.30) on page 279 in R9 (refer also to Appendices A and B in R9). The no-slip condition is used at the wall for the velocity components. The numerical procedures are described in R9 on page 283 and further details on the physics of the formation of the Klebanoff modes, besides the ones in LWG99 and R9, are found in Ricco [41].

## 4 Experimental results

### *4.1 Time-averaged statistics of streaks*

As predicted by the Goldstein theory (LWG99), the instantaneous time traces (not shown) indicate that the largest velocity fluctuations are measured in the boundary-layer core. The energy spectra at different wall-normal positions reveal that in the boundary-layer core the low-frequency structures, i.e., the laminar streaks, are amplified and the high-frequency ones are damped with respect to the free stream. This phenomenon of the boundary layer behaving as a filter to the high-frequency free-stream fluctuations was previously termed shear sheltering [20].

The instantaneous time trace $u^*(t^*)$ is divided in positive and negative fluctuations with respect to the local time-averaged value, $\overline{u}^*$. The same definition has been employed by Asai *et al.* [3]. The positive and negative streaks are therefore defined as follows,

$$\left.\begin{array}{l} u^*_{pos} : u'^*(t^*) > \overline{u^*(t^*)} \\ u^*_{neg} : u'^*(t^*) < \overline{u^*(t^*)}. \end{array}\right\} \tag{12}$$

The rms, skewness $\mathcal{S}$, and third moment $\mathcal{T}$ are calculated from the full velocity signal, and from the positive and negative streaks separately (95% percentile of the full signal is considered, as in [29]).

Figure 3 shows the statistics of the full signal of the streamwise velocity and of the positive and negative streaks. Figure 3a) shows the rms of the scaled velocity. In agreement with previous studies [33], its maximum is at $y^*/\delta^*$ =1.3-1.4, where the boundary-layer thickness $\delta^*$ is the wall-normal location where the mean velocity is $0.99U^*_\infty$. In the outer region, $y^*/\delta^*$>1, the rms of the negative streaks is larger than the one of the positive streaks. As the free stream is approached, the rms values reach the same level. The maxima of the positive and negative streak rms levels are located at different wall-normal positions. This observation may explain the double maximum in the rms profiles found in other experiments, i.e., the data shown in figure 9 on page 208 in [56].

The skewness of the signals, shown in figure 3b), gives a clear indication of the boundary-layer locations at which the positive and negative streaks dominate. While in figure 3a) it is not evident which of the two is more significant near the wall, the skewness profiles distinctly show that the positive fluctuations dominate for $y^*/\delta^*$<1.

Another good measure of the positive and negative streaks is the third moments, shown in figure 3c). Close to the wall, the value is almost zero indicating that the fluctuation level in this high-shear region is low, despite the high skew. The high skew is caused by the low rms level close to the wall. This

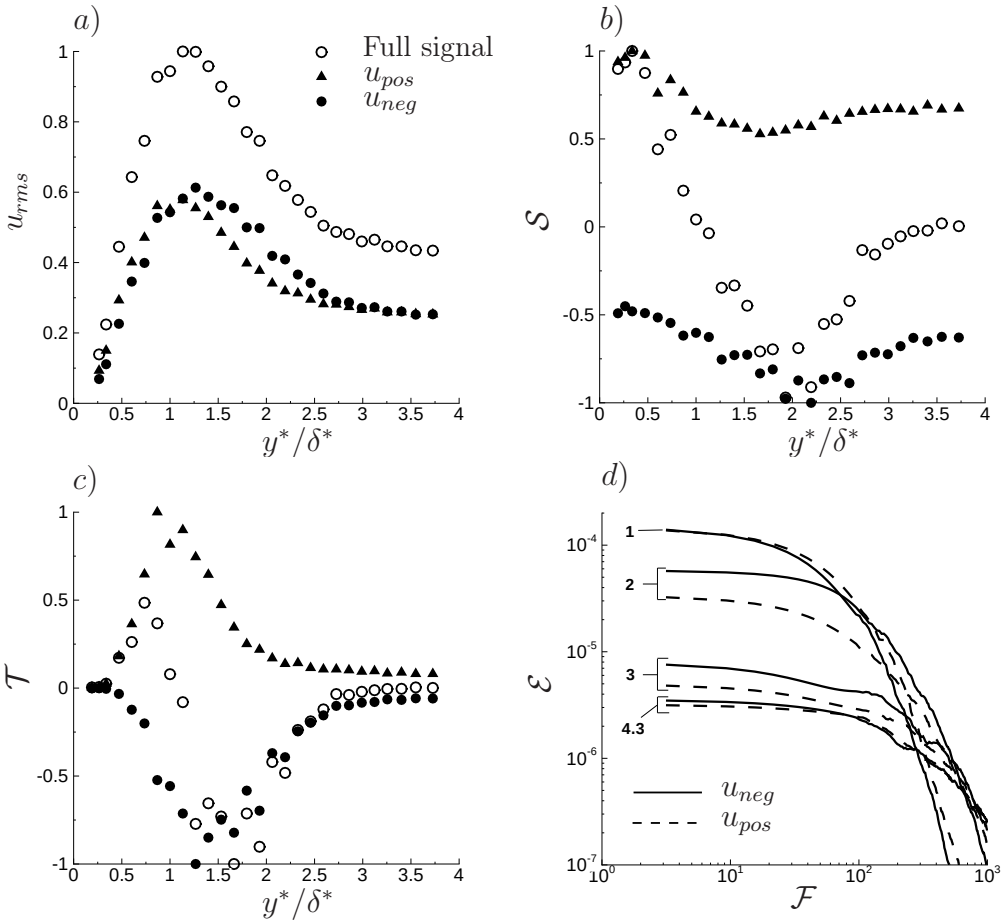


Figure 3. Statistics of full signal, positive and negative fluctuations within the boundary layer at $x^*$=192 mm ($Re_\theta$ = 130). a) Rms; b) skewness; c) third moment; d) energy spectra. The numbers in graph d) indicate $y^*/\delta^*$.

illustrates that the near-wall flow is mildly altered in terms of fluctuations by the presence of free-stream turbulence, similar to that of the viscous sub-layer of a turbulent boundary layer.

Figure 3d) presents the spectra of the positive (dashed lines) and negative streaks (solid lines). Near the wall at $y^*/\delta^*$ =1, the positive streaks contain slightly more energy than the negative ones for frequencies $\mathcal{F}=2\pi f^*\nu^*10^6/U_\infty^{*2}$ >10. At $y^*/\delta^*$ =2, the negative streaks have higher energy content at the low frequencies and lower energy at higher frequencies. Near the free stream, at $y^*/\delta^*$ =4.3, the energy within the positive and negative streaks is almost identical, which is expected as the flow becomes more isotropic.

### *4.2 Maximum streamwise streak velocity*

Although the time-averaged representation of the positive and negative streaks provides insight into the flow physics, it is unlikely that this approach would identify the details of the breakdown process. One hypothesis may be that the only streaks leading to turbulent spots are those with the velocity perturbation

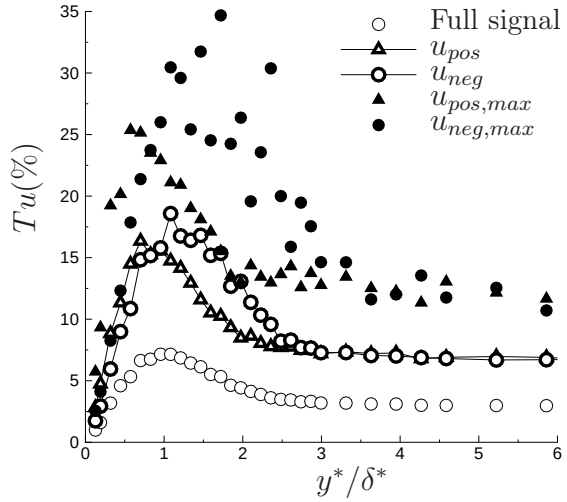


Figure 4. Root-mean-square value of the full signal, of the signal of the positive and negative fluctuations, and of the maxima of the positive and negative fluctuations.

levels higher than a threshold as it has been shown that low-energy streaks do not become turbulent spots [30]. Therefore, it is interesting to study the largest values of velocity perturbations.

Figure 4 shows the percentage intensity as functions of the wall-normal coordinate of the full time signal of the streamwise velocity fluctuations, and of the positive and negative streaks. Near the wall, positive streaks have higher magnitudes than the negative streaks and the opposite is true near the free stream. The peak positive fluctuations can be five times higher than the full-signal average, while the peak of the negative fluctuations can exceed the full-signal average by six-seven times. The peak of the negative fluctuations can be double the peak of the positive fluctuations in the outer part of the boundary layer.

Figure 5 (left) shows the downstream growth of the maximum values across the boundary layer of the time-averaged $u_{rms}$, maximum positive and negative velocity perturbations, and the 99% and 1% levels as functions of $Re_\theta$. The rms varies approximately linearly with $Re_\theta$ (i.e., with the square root of $Re_x$=$U^*_\infty x^*/\nu^*$), in agreement with previous experiments [33, 11]. As shown in figure 5 (right), where the data are normalized by the values at the last measurement location, the positive and negative velocity perturbations also scale linearly and have the same scaled growth rate of the rms for $Re_\theta$>90.

### *4.3 Frequency content of streaks*

The interest in this section is on the wall-normal distribution of streak energy at specified frequencies and on their downstream evolution. Figure 6 shows the energy content at $x^*$=40 mm ($Re_\theta = 60$) (left) and at $x^*$=275 mm ($Re_\theta = 161$)

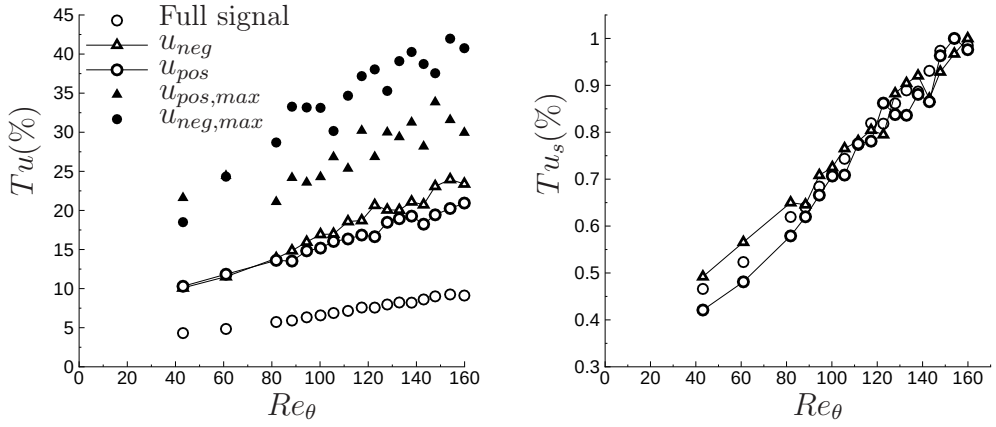


Figure 5. Left: streamwise growth rates of maximum intensity of streamwise velocity perturbations within the boundary layer. Right: growth rates scaled by their maximum values (the subscript $s$ denotes this scaling).

(right). As also shown in figure 3, the main contribution to $u_{rms}$ is from the lowest frequencies, $\mathcal{F}$<150 ($f^*$<15Hz), and this contribution increases as the flow evolves downstream. The disparity in magnitude amplifies downstream as disturbances with the highest frequency decay ($\mathcal{F}$=610), penetrating less into the boundary layer and showing no peak value within the boundary layer. The high-frequency disturbances decay downstream much more in the boundary-layer core than near the free stream. The peak energy is about $y^*/\delta^*$ =1.4 for $\mathcal{F}$<300 at $x^*$=40 mm, while at $x^*$ = 275 mm the peak of lowest frequencies moves closer to the wall at about $y^*/\delta^*$ =1 and the peak of the higher frequencies moves towards the free stream. For $\mathcal{F}$=3, there is over an order of magnitude energy increase near the wall, while for $\mathcal{F}$=610, there is an order of magnitude energy reduction near the wall. The inset of figure 6 shows $\mathcal{G}$, the ratio of maximum energy at $x^*$=40 mm and $x^*$=275 mm, as a function of the frequency $\mathcal{F}$. The maximum growth rate is inversely proportional to the frequency.

Figure 7 (left) shows the downstream growth of the peak full-signal energy values at different frequencies, and figure 7 (right) the same quantity for the negative fluctuations (the energy of the positive fluctuations is not shown). For $\mathcal{F} < 100$, the disturbances again show an intense growth, while for $\mathcal{F} > 150$, the disturbance energy decays. The negative and positive streaks display the same trends, although the negative streaks at high frequency, $\mathcal{F}$= 610, drop substantially faster than their positive counterpart.

These growth and decay rates are quantified in Table 2, which summarizes the constants of the exponential curve fit to all the frequencies of figure 7 with an equation of the form $\mathcal{E} = \mathcal{A}(Re_x^{0.5})^{\mathcal{B}}$. The equation for the $\mathcal{F} = 46$ results in a nearly linear relationship between $\mathcal{E}$ and $Re_x$, which is the same result found in figure 5 (left) when the whole spectrum was considered through $u_{rms}$.

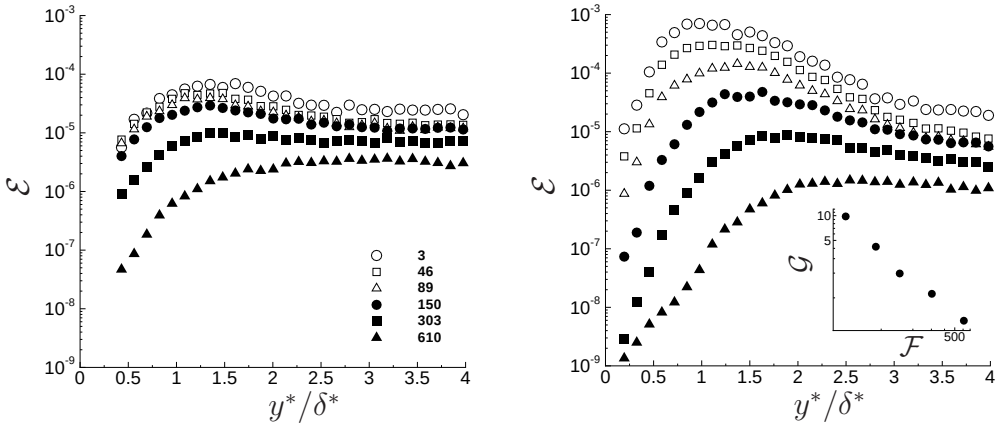


Figure 6. Energy content at different frequencies $\mathcal{F}$, given in the legend of the left graph. Left: $x^*$= 40mm ($Re_\theta$ = 60). Right: $x^*$= 275mm ($Re_\theta$ = 161). The inset shows $\mathcal{G}$, the ratio of growth rates of the maximum energy from $x^*$=40 mm to $x^*$=275 mm, as a function of the frequency $\mathcal{F}$.

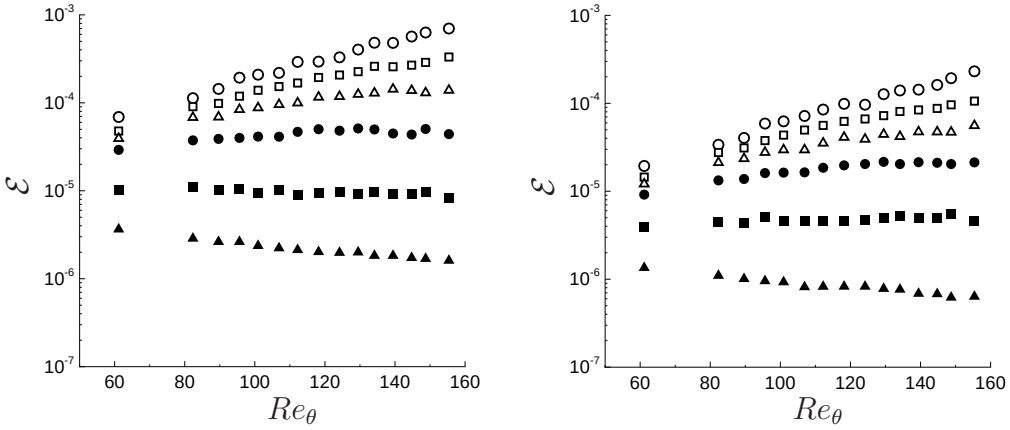


Figure 7. Growth of maximum energy content along the streamwise direction. Left: full signal. Right: negative streaks. The legend is the same as in figure 6.

| | Full signal | | Negative | | Positive | |
|---|---|---|---|---|---|---|
| $\mathcal{F}$ | $\mathcal{A}$ | $\mathcal{B}$ | $\mathcal{A}$ | $\mathcal{B}$ | $\mathcal{A}$ | $\mathcal{B}$ |
| 3 | 1.6$E$-10 | 2.8 | 5 $E$-11 | 2.8 | 4.5$E$-11 | 2.8 |
| 46 | 6$E$-9 | 2.0 | 1.1 $E$-9 | 2.1 | 3$E$-9 | 1.9 |
| 89 | 2.1$E$-7 | 1.2 | 2.5 $E$-8 | 1.4 | 1.06$E$-7 | 1.1 |
| 150 | 7.1$E$-6 | 0.35 | 3 $E$-6 | 0.8 | 3$E$-6 | 0.3 |
| 303 | 4.2$E$-5 | -0.28 | 1.7 $E$-6 | 0.2 | 2.7$E$-5 | -0.4 |
| 610 | 3.6$E$-4 | -1.0 | 5.3 $E$-5 | -0.8 | 8$E$-6 | -0.4 |

Table 2
Exponential constants to represent the data of figure 7, with the form $\mathcal{E} = \mathcal{A}(Re_x^{0.5})^{\mathcal{B}}$.

## 5 Validation of theoretical results against experimental and direct numerical simulations results

The objective of this section is to compare the wall-normal profiles of the streak streamwise velocity computed by solving the unsteady boundary region equations with our experimental profiles and with the rms profiles obtained by the DNS carried out by Wu & Moin [59] (figure 29 on page 33 in their paper). In [59], bypass transition to turbulence is induced in a flat-plate Blasius boundary layer by periodically passing free-stream patches of turbulence.

As evident from the profiles at $x^*$=40 mm ($Re_\theta = 60$) in figure 6 and from the DNS profiles shown by Wu & Moin, the energy content in the outer portion of the boundary layer is comparable with the content in the boundary-layer core. Therefore, it is essential to combine the LWG99 theory, which describes the streaks in the boundary-layer core, and the R9 theory, which describes the leading-order behaviour in the outer portion of the boundary layer.

As our experimental data and Wu & Moin's data were obtained through the free-stream forcing of full-spectrum turbulence while our numerical results correspond to the evolution of a single Fourier mode, a few assumptions are to be advanced for a meaningful comparison. The key objective is to find the Fourier mode that is most responsible for the growth of the streaks inside the boundary layer. Thanks to these assumptions, described in the following, the number of free parameters is kept to a minimum.

### *5.1 Assumptions and estimation of flow quantities*

- *Small-amplitude fluctuations*
  It is assumed that the boundary-layer fluctuations can be treated as linearized perturbations about the Blasius flow. For our experiments, this is reasonable at $x^* = 40$ mm ($Re_\theta = 60$) and $x^* = 275$ mm ($Re_\theta = 161$) because these locations are upstream of the beginning of the transition region, where nonlinear effects dominate. For the DNS profiles, it is clear that nonlinear interactions are absent at the downstream locations of the profiles in figure 29 of Wu & Moin's paper [59] because their mean velocity profile agrees with the Blasius profile (refer also to figure 8 on page 19 in [59]).

  Under this assumption, each vortical structure corresponds to a Fourier mode and is assumed to evolve independently. For our experiments, the gust-convection relation, $k_x^*=2\pi f^*/U_\infty^*=2\pi/\lambda_x^*$, is thus assumed to hold. For the DNS results, the dominant streamwise length scale is the streamwise distance between the free-stream passing patches of turbulence, which can be estimated from figure 1 on page 10 in [59]. We assume that this distance is of the same order as the streamwise wavelength of the representative free-stream gust, $\lambda_x^*$, which allows computing $\overline{x} = 2\pi x^*/\lambda_x^*$. We focus on our experimental profiles for $\mathcal{F} = 3$ and $\mathcal{F} = 303$ at $x^*$ =40 mm ($Re_\theta = 60$) and $x^*$ =275 mm ($Re_\theta = 161$), and on the DNS profiles in figure 29 in [59].
- *Axial-symmetric turbulence in $y - z$ plane*

It is assumed that the free-stream turbulence is axial-symmetric, i.e., homogeneous and isotropic in $y-z$ planes perpendicular to the mean flow [4, 8]. In our experiments, this assumption is reasonable because the free-stream flow is generated by a rigid grid with equal spacing along the wall-normal and spanwise directions. Therefore, vortical structures which are symmetric along these two directions are generated. In the DNS, the free-stream turbulence is isotropic in $y-z$ planes perpendicular to the mean flow. It is thus assumed that $\lambda_y^*{=}\lambda_z^*$ ($\kappa_y{=}k_y/\sqrt{k_x R_\lambda}{=}\kappa$) and $\hat{u}_y^\infty{=}\hat{u}_z^\infty$, defined in (4).

- *Estimation of spanwise wavelength*

  The spanwise wavelength $\lambda_z^*$ must also be estimated. For both the experiments and the DNS, $\lambda_z^*$ is estimated through the decay rate of the free-stream disturbances. According to linear theory, a free-stream gust modelled by a single Fourier component decays exponentially along the streamwise direction because of viscous effects along the wall-normal and spanwise directions. The free-stream decay rate is $\exp\left[-(\kappa^2+\kappa_y^2)\overline{x}\right]$, which is evident from the outer free-stream boundary conditions for the boundary-region equations, given in (5.29) and (5.30) on page 183 in LWG and in (2.13) and (2.21)-(2.23) on pages 277 and 278 in R9. By use of the definitions of the scaled wavenumbers $\kappa$ and $\kappa_y$ and of the scaled streamwise coordinate $\overline{x}$, the spanwise wavelength is estimated as follows:

$$\lambda_z^* = 2\pi\sqrt{\frac{2\nu^*\Delta x^*}{U_\infty^*\ln(u_r)}},$$

  where $u_r$ is the ratio of the free-stream perturbation velocities at the two downstream locations between which the viscous decay is considered, i.e., $x^*$ =40 mm ($Re_\theta = 60$) and $x^*$ =275 mm ($Re_\theta = 161$) for our experiments and $Re_\theta = 100$ and $Re_\theta = 180$ for the DNS. The only parameters estimated through fitting the experimental data are therefore $\hat{u}_x^\infty$ and $\hat{u}_z^\infty$.

  Note that, although different values for $\hat{u}_x^\infty$ and $\hat{u}_z^\infty$ are estimated for different frequencies in our experiments, the same values are used at the different $x$ locations as the change in the free stream along this direction is accounted for by the exponential decay due to viscous effects.

For our experimental results, it is found that for $\mathcal{F} = 3$, $\lambda_z^* = 24$ mm, $\kappa$=0.72, $\hat{u}_x^\infty = 1$ and $\hat{u}_z^\infty = 0.35$, and, for $\mathcal{F} = 303$, $\lambda_z^* = 14$ mm, $\kappa$=0.09, $\hat{u}_x^\infty = 0.15$ and $\hat{u}_z^\infty = 0.03$. For the DNS results, it is found that $\kappa$=0.38, $k_x$ =0.08, $\hat{u}_x^\infty = 15$ and $\hat{u}_z^\infty = 1$.

### *5.2 Results*

Figure 8 presents the comparison between the experimental profiles and the numerical calculations of the boundary-region solution $\overline{u}_0$, given by the first expression in (9). The overall agreement of the trends is good, which further confirms the validity of the LWG99 and R9 theories. The match between our calculations and the experimental data is better than in the comparison

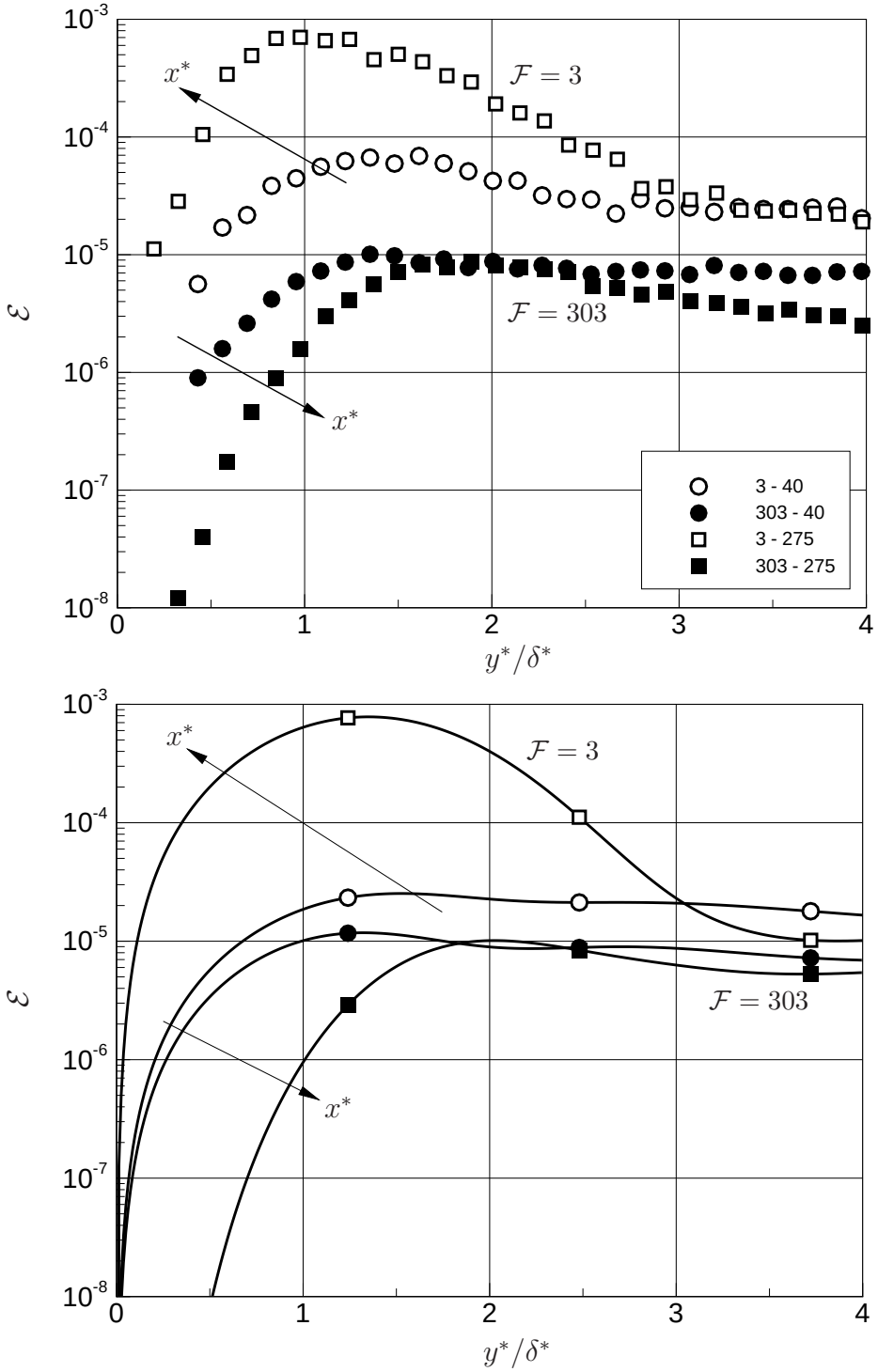


Figure 8. Comparison between experimental (top) and numerical (bottom) energy disturbance profiles for $\mathcal{F} = 3$ and $\mathcal{F} = 303$ at $x^*$ =40 mm ($Re_\theta = 60$) and $x^*$ =275 mm ($Re_\theta = 161$). In the legend, the first number indicates the frequency $\mathcal{F}$ and the second number denotes the location $x^*$.

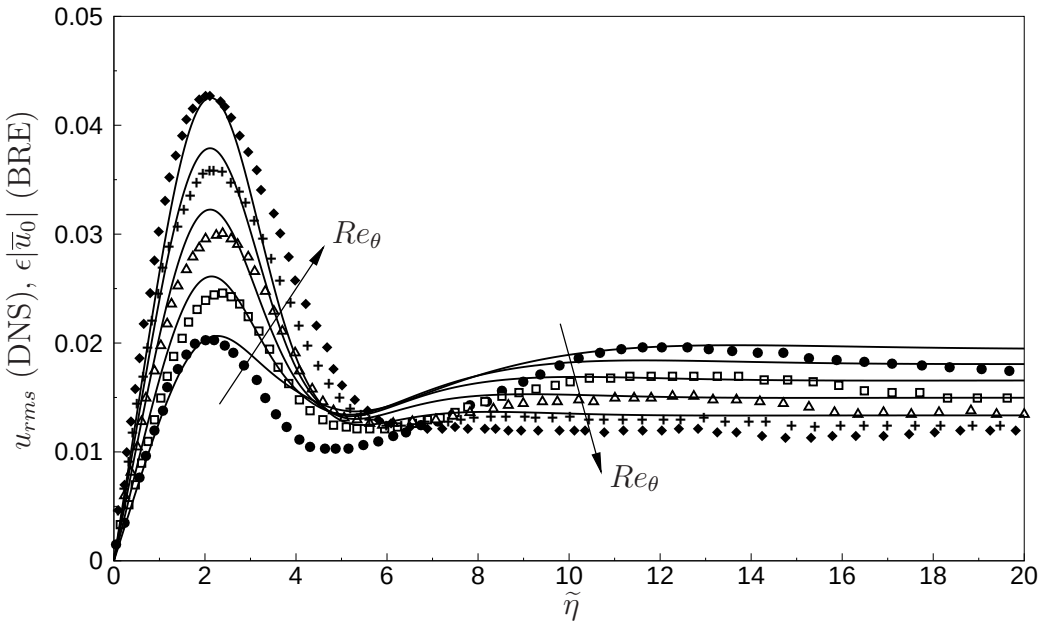


Figure 9. Comparison between the DNS profiles from figure 29 on page 33 in Wu & Moin [59] (symbols) and the solutions of the boundary-region equations (BRE in the label) given by (9) (lines). Symbols: circles, $Re_\theta = 100$; squares, $Re_\theta = 120$; triangle, $Re_\theta = 140$; plus, $Re_\theta = 160$; diamond, $Re_\theta = 180$. The beginning of the transition to turbulence is at $Re_\theta$ =200. The wall-normal coordinate is $\widetilde{\eta} = y^*\sqrt{U^*_\infty/\nu^* x^*}$, as in Wu & Moin [59].

between Westin *et al.* [56] and the boundary-region solutions, presented by R9, especially in the outer layer, where $\overline{u}^{(0)}$ is of leading order.

Figure 9 shows the comparison between Wu & Moin's DNS data (symbols) and our boundary-region calculations (lines). The wall-normal locations of the maxima in the boundary-layer core, the downstream growth of the laminar streaks, and the local minima in the outer portion of the boundary layer are captured satisfactorily. Two main disagreements between the profiles are worth discussing. The profiles at the location closest to the leading edge (black circles) show excellent agreement up to $\tilde{\eta} = 2$, whereas at higher locations the DNS data present a more marked local minimum than the boundary-region ones. This mismatch near the free stream is likely to be due to our simplified model of the passing turbulent patches by a convected gust. Near the leading edge the laminar streaks have not grown to a sufficient magnitude and therefore the outer flow plays a dominant role [42]. At the furthermost streamwise location and near the free stream the DNS profiles (black diamonds) are more intense than the boundary-region profiles because the nonlinear effects, which are not included in our formulation, start to exert their influence as this is the location closest to the transition point. It has indeed been shown by experiments [33] (figure 2c on page 156) and by Ricco *et al.* [44] (figure 10a on page 21) that in a pre-transitional boundary layer nonlinear vortical interactions

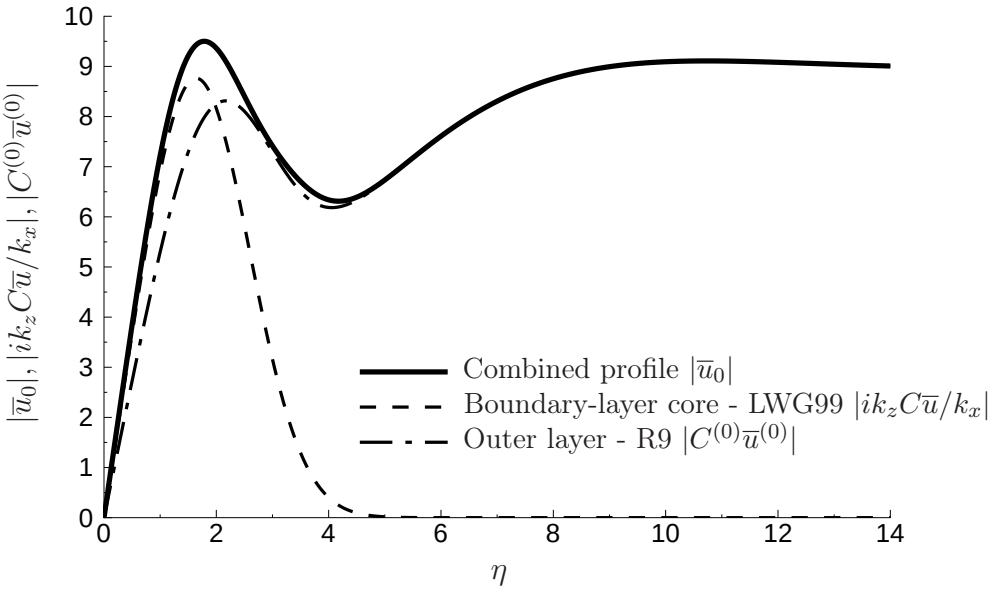


Figure 10. Wall-normal profiles of the streamwise velocity perturbation computed by solving the boundary-region equations given on page 180 in LWG99 at $Re_\theta = 100$ for the same conditions as in figure 9. The solid line shows the combined profile $|\overline{u}_0|$, the dashed line shows the component $|ik_z C\overline{u}/k_x|$, and the dash-dotted line indicates the component $|C^{(0)}\overline{u}^{(0)}|$, all given in (9). The quantities $C$ and $C^{(0)}$ are defined in (11).

cause an increase in fluctuation intensity in the outer region of the boundary layer.

Wu & Moin [59] correctly demonstrated that the transition mechanism is not caused by Tollmien-Schlichting waves and recognized that a bypass transition process must be at work. The comparison in figure 9 proves that the breakdown to turbulence is initiated through the growth of the laminar streaks, whose dynamics is described mathematically by the LWG99 and R9 theories.

Figure 10 shows the relative contributions to the full streak profile of the boundary-layer core component $\overline{u}$ (dashed line), described by the LWG99 theory, and the outer-layer component $\overline{u}^{(0)}$ (dash-dotted line), described by R9 theory, at $Re_\theta = 100$. As predicted by the asymptotic theory, $\overline{u}^{(0)}$ is dominant in the outer portion of the boundary layer. It also offers a significant contribution in the core of the boundary layer, which demonstrates that LWG99's $\overline{u}$ component and R9's $\overline{u}^{(0)}$ component must be employed together to describe the streak dynamics at this downstream location.

The LWG99 and R9 theories provide a firm basis for describing the laminar streaks at the early stages of the evolution and further effort is needed to predict the initiation of transition due to free-stream turbulence. A first step

in this direction can be taken by solving the nonlinear boundary region equations forced by full-spectrum turbulence and by carrying out the secondary instability analysis of the nonlinearly-saturated Klebanoff modes.

## 6 Summary and concluding remarks

In this paper, we have studied a pre-transitional flat-plate boundary layer perturbed by free-stream turbulence. The four most relevant theoretical frameworks describing the Klebanoff modes have been thoroughly discussed and parallels and complimentary aspects of the theories have been pointed out. This discussion has supported our choice to use the Goldstein theory [26].

We have observed that the level of instantaneous streaky perturbations are much larger than the time-averaged velocities and that the positive streaks are more energetic closer to the wall and negative streaks are more intense near the free stream. It was found that the rms level and the maximum perturbations of positive and negative streaks grow downstream at approximately the same rate.

The time signal of the streak velocity was divided into discrete frequency bands to examine the streamwise evolution of the perturbations in each band. As the flow evolves downstream, the maximum values in the lower frequency bands move slightly towards the wall, while those in the high frequency bands move towards the free stream. For the first time, the growth rates of the maximum energy level have been computed to quantify how low-frequency disturbances amplify and how higher-frequency disturbances decay as the flow evolves downstream. It was also found that the growth rate of medium-low frequency was proportional to the growth rate of the $u_{rms}$.

Finally, we have compared our asymptotic numerical solutions with streak profiles measured in the wind tunnel and computed through DNS [59]. We have shown that the theoretical frameworks developed by LWG99 and R9 successfully predict these profiles across the whole wall-normal extent of the boundary layer, despite the simplifying assumptions adopted in the theoretical formulation, described in §5. Amongst these, the most significant simplification is arguably the hypothesis that the free-stream turbulence is axial-symmetric and that it can be represented by a dominant Fourier mode with equal wavelengths along the wall-normal and spanwise directions.

Future lines of research should be directed to the dependence of the nonlinear streaks on the characteristics of the free-stream flow, on the estimation of the transition location for different free-stream flows, and on more controlled experimental campaigns for further validation of the theoretical framework employed in this paper.

**Acknowledgements**

PR's research work was partially funded by EPSRC First Grant EP/I033173/1. The contributions of DMM were partly supported by the Experimental Program to Stimulate Competitive Research under Award DE-SC0004751 (U.S. Department of Energy) and by the Center for Advanced Energy Studies via U.S. Department of Energy Idaho Operations Office Contract DE-AC07-05ID14517. Accordingly, the U.S. Government retains a nonexclusive, royalty-free license to publish or reproduce the published form of this contribution, or allow others to do so, for U.S. Government purposes.

## References

[1] B.J. Abu-Ghannam and R. Shaw. Natural transition of boundary-layers - the effects of turbulence, pressure-gradient, and flow history. *J. Mech. Eng. Sci.*, 22:213–228, 1980.

[2] P. Andersson, M. Berggren, and D.S. Henningson. Optimal disturbances and bypass transition in boundary layers. *Phys. Fluids*, 11(1):134–150, 1999.

[3] M. Asai, M. Minagawa, and M. Nishioka. The instability and breakdown of a near-wall low-speed streak. *J. Fluid Mech.*, 455:289–314, 2002.

[4] G.K. Batchelor. The theory of axisymmetric turbulence. *Proc. R. Soc. London A*, 186(1007):480–502, 1946.

[5] G.K. Batchelor. *An Introduction to Fluid Dynamics*. Cambridge University Press, 1967.

[6] L. Brandt, P. Schlatter, and D.S. Henningson. Transition in boundary layers subject to free-stream turbulence. *J. Fluid Mech.*, 517:167–198, 2004.

[7] F. Brighenti. *On the experimental receptivity in a pre-transitional laminar boundary layer*. PhD thesis, College of Engineering, University of Limerick, 2013.

[8] S. Chandrasekhar. The theory of axisymmetric turbulence. *Proc. R. Soc. London A*, 242(855):557–577, 1950.

[9] G. Comte-Bellot and S. Corrsin. The use of a contraction to improve the isotropy of grid-generated turbulence. *J. Fluid Mech.*, 25:657–682, 1966.

[10] M. Dong and X. Wu. On continuous spectra of the Orr-Sommerfeld/Squire equations and entrainment of free-stream vortical disturbances. *J. Fluid Mech.*, 2013.

[11] J.H.M. Fransson, M. Matsubara, and P.H. Alfredsson. Transition induced by free-stream turbulence. *J. Fluid Mech.*, 527:1–25, 2005.

[12] W.K. George. The decay of homogeneous isotropic turbulence. *Phys. Fluids*, 4(7):1492–1509, 1992.

[13] M.E. Goldstein. Effect of free-stream turbulence on boundary layer transition. *Phil. Trans. Royal Soc.*, 372(2020):20130354, 2014.

[14] J. Groth and A.V. Johansson. Turbulence reduction by screens. *J. Fluid Mech.*, 197:139–155, 1988.

[15] A.N. Gulyaev, V.E. Kozlov, V.R. Kuzenetsov, B.I. Mineev, and A.N. Sekundov. Interaction of a laminar boundary layer with external turbulence. *Fluid Dynamics. Translated from Izv, Akad. Navk. SSSR Mekh. Zhid. Gaza 6, vol. 5, pp. 55-65.*, 24(5):700–710, 1989.

[16] D. Hernon, E.J. Walsh, and D.M. McEligot. Experimental investigation into the routes to bypass transition and the shear-sheltering phenomenon. *J. Fluid Mech.*, 591:461–479, 2007.

[17] D. Hernon, E.J. Walsh, and D.M. McEligot. Instantaneous fluctuation velocity and skewness distributions upstream of transition onset. *Int. J. Heat Fluid Flow*, 28:1272–1279, 2007.

[18] M. Higuera and J.M. Vega. Modal description of internal optimal streaks. *J. Fluid Mech.*, 626:21–31, 2009.

[19] J. Hourmouziadis. Aerodynamic design of of low pressure turbines. *AGARD Lecture Series*, 167, 1989.

[20] R.G. Jacobs and P.A. Durbin. Simulation of bypass transition. *J. Fluid Mech.*, 428:185–212, 2001.

[21] J.M. Kendall. Boundary layer receptivity to free stream turbulence. *AIAA Paper*, 90-1504, 1990.

[22] P.S. Klebanoff. Effect of free-stream turbulence on a laminar boundary layer. *Bull. Am. Phys. Soc.*, 16:1323, 1971.

[23] T. Kurian and J.H.M. Fransson. Grid-generated turbulence revisited. *Fluid Dyn. Res.*, 41(021403), 2009.

[24] S. Lardeau, N. Li, and M.A. Leschziner. Large eddy simulations of a transitional boundary layer at high free-stream turbulence intensity and implications for RANS modelling. *J. Turbom.*, 129:1–7, 2007.

[25] E.M. Laws and J.L. Livesey. Flow through screens. *Ann. Rev. Fluid Mech.*, 10:247–266, 1978.

[26] S.J. Leib, D.W. Wundrow, and M.E. Goldstein. Effect of free-stream turbulence and other vortical disturbances on a laminar boundary layer. *J. Fluid Mech.*, 380:169–203, 1999.

[27] P. Luchini. Reducing the turbulent skin friction. In J.A. Desideri et al. – Wiley, editor, *Computational Methods in Applied Sciences – Proc. 3rd ECCOMAS CFD Conference*, pages 466 – 470, 1996.

[28] P. Luchini. Reynolds-number-independent instability of the boundary layer over a flat surface: optimal perturbations. *J. Fluid Mech.*, 404:289–309, 2000.

[29] A.C. Mandal, L. Venkatakrishnan, and J. Dey. A study on boundary-layer transition induced by free-stream turbulence. *J. Fluid Mech.*, 660:114–146, 2010.

[30] J. Mans, E.C. Kadijk, H.C. de Lange, and A.A. van Steenhoven. Breakdown in a boundary layer exposed to free-stream turbulence. *Exp. Fluids*, 39:1071–1083, 2005.

[31] J.A. Martín and C. Martel. Nonlinear streak computation using boundary

region equations. *Fluid Dyn. Res.*, 44(045503):1–23, 2012.
[32] J.A. Martín and C. Martel. Nonlinear intrinsic streaks in the flat plate boundary layer. *Aero. Sc. Tech.*, 44:101–107, 2015.
[33] M. Matsubara and P.H. Alfredsson. Disturbance growth in boundary layers subjected to free-stream turbulence. *J. Fluid Mech.*, 430:149–168, 2001.
[34] R.E. Mayle. The role of laminar-turbulent transition in gas turbine engines. *J. Turbom.*, 113(4):509–537, 1991.
[35] F.R. Menter, R. Langtry, and S. Volker. Transition modelling for general purpose CFD codes. *Flow Turb. Comb.*, 77(1-4):277–303, 2006.
[36] M.S. Mohamed and J.C. LaRue. The decay power law in grid-generated turbulence. *J. Fluid Mech.*, 219:195–214, 1990.
[37] K.P. Nolan, E.J. Walsh, and D.M. McEligot. Quadrant analysis of a transitional boundary layer subject to free-stream turbulence. *J. Fluid Mech.*, 658:310–335, 2010.
[38] K.P. Nolan and T.A. Zaki. Conditional sampling of transitional boundary layers in pressure gradients. *J. Fluid Mech.*, 728:306–339, 2013.
[39] D.A. Pook, J.H. Watmuff, and A.C. Orifici. Test section streaks originating from imperfections in a zither located upstream of a contraction. *J. Fluid Mech.*, 787:254–291, 2016.
[40] S.B. Pope. *Turbulent Flows*. Cambridge University Press, 2000.
[41] P. Ricco. Asymptotic theory of the pre-transitional laminar streaks and comparison with experiments. In *7th IUTAM Symposium on Laminar-Turbulent Transition, June 23-26, 2009 Stockholm*, 2009.
[42] P. Ricco. The pre-transitional Klebanoff modes and other boundary layer disturbances induced by small-wavelength free-stream vorticity. *J. Fluid Mech.*, 638:267–303, 2009.
[43] P. Ricco and F. Dilib. The influence of wall suction and blowing on laminar boundary-layer streaks generated by free-stream vortical disturbances. *Phys. Fluids*, 22(044101), 2010.
[44] P. Ricco, J. Luo, and X. Wu. Evolution and instability of unsteady nonlinear streaks generated by free-stream vortical disturbances. *J. Fluid Mech.*, 677:1–38, 2011.
[45] P. Ricco, D. Shah, and P.D. Hicks. Compressible laminar streaks with wall suction. *Phys. Fluids*, 25(054110), 2013.
[46] P. Ricco, D.-L. Tran, and G. Ye. Wall heat transfer effects on Klebanoff modes and Tollmien-Schlichting waves in a compressible boundary layer. *Phys. Fluids*, 21(024106), 2009.
[47] P. Ricco and X. Wu. Response of a compressible laminar boundary layer to free-stream vortical disturbances. *J. Fluid Mech.*, 587:97–138, 2007.
[48] P. Roach. The generation of nearly isotropic turbulence by means of grids. *Int. J. Heat Fluid Flow*, 8:82–92, 1987.
[49] G.B. Schubauer and H.K Skramstad. Laminar boundary-layer oscillations and stability of laminar flow. *J. Aero. Sc.*, 14(2):69–78, 1947.
[50] K. Stewartson. On asymptotic expansion in the theory of boundary layer.

*J. Math. Phys.*, 36:137, 1957.

[51] G.I. Taylor. The spectrum of turbulence. *Proc. Roy. Soc. Lond. A*, 164:476–490, 1938.

[52] G.I. Taylor. Some recent developments in the study of turbulence. *Fifth Intl. Congr. for Appl. Mech. (ed. J.P. Den Hartog & Peters) - Wiley/Chapman and Hall, New York-London*, pages 294–310, 1939.

[53] H. Tennekes and J.L. Lumley. *A First Course in Turbulence*. MIT Press, 1970.

[54] R. Tresso and D.R. Munoz. Homogeneous, isotropic flow in grid generated turbulence. *J. Fluids Eng.*, 122:51–56, 2000.

[55] E.J. Walsh, D. Hernon, M.R.D. Davies, and D.M. McEligot. Preliminary measurements from a new flat plate facility for aerodynamic research. In *Proc. 6th Europ. Conf. on Turbomachinery*, 2005.

[56] K.J.A. Westin, A.V. Boiko, B.G.B. Klingmann, V.V. Kozlov, and P.H. Alfredsson. Experiments in a boundary layer subjected to free stream turbulence. Part 1. Boundary layer structure and receptivity. *J. Fluid Mech.*, 281:193–218, 1994.

[57] X. Wu and M. Choudhari. Linear and non-linear instabilities of a Blasius boundary layer perturbed by streamwise vortices. Part 2. Intermittent instability induced by long-wavelength Klebanoff modes. *J. Fluid Mech.*, 483:249–286, 2003.

[58] X. Wu and J. Luo. Linear and non-linear instabilities of a Blasius boundary layer perturbed by streamwise vortices. Part 1. Steady streaks. *J. Fluid Mech.*, 483:225–248, 2003.

[59] X. Wu and P. Moin. Direct numerical simulation of turbulence in a nominally zero-pressure-gradient flat-plate boundary layer. *J. Fluid Mech.*, 630:5–41, 2009.

[60] D.W. Wundrow and M.E. Goldstein. Effect on a laminar boundary layer of small-amplitude streamwise vorticity in the upstream flow. *J. Fluid Mech.*, 426:229–262, 2001.

[61] T. Zhou, R.A. Antonia, L. Danaila, and F. Anselmet. Transport equations for the mean energy and temperature dissipation rates in grid turbulence. *Exp. Fluids*, 28:143–151, 2000.